NASA/TM—2017-219703

The Effects of Fiber Orientation and Adhesives on Tensile Properties of Carbon Fiber Reinforced Polymer Matrix Composite With Embedded Nickel-Titanium Shape Memory Alloys

Derek J. Quade
Glenn Research Center, Cleveland, Ohio

Sadhan C. Jana, Gregory N. Morscher, and Manigandan Kannan
University of Akron, Akron, Ohio

Linda S. McCorkle
Ohio Aerospace Institute, Brook Park, Ohio

November 2017

NASA STI Program . . . in Profile

Since its founding, NASA has been dedicated to the advancement of aeronautics and space science. The NASA Scientific and Technical Information (STI) Program plays a key part in helping NASA maintain this important role.

The NASA STI Program operates under the auspices of the Agency Chief Information Officer. It collects, organizes, provides for archiving, and disseminates NASA's STI. The NASA STI Program provides access to the NASA Technical Report Server—Registered (NTRS Reg) and NASA Technical Report Server—Public (NTRS) thus providing one of the largest collections of aeronautical and space science STI in the world. Results are published in both non-NASA channels and by NASA in the NASA STI Report Series, which includes the following report types:

- TECHNICAL PUBLICATION. Reports of completed research or a major significant phase of research that present the results of NASA programs and include extensive data or theoretical analysis. Includes compilations of significant scientific and technical data and information deemed to be of continuing reference value. NASA counter-part of peer-reviewed formal professional papers, but has less stringent limitations on manuscript length and extent of graphic presentations.

- TECHNICAL MEMORANDUM. Scientific and technical findings that are preliminary or of specialized interest, e.g., "quick-release" reports, working papers, and bibliographies that contain minimal annotation. Does not contain extensive analysis.

- CONTRACTOR REPORT. Scientific and technical findings by NASA-sponsored contractors and grantees.

- CONFERENCE PUBLICATION. Collected papers from scientific and technical conferences, symposia, seminars, or other meetings sponsored or co-sponsored by NASA.

- SPECIAL PUBLICATION. Scientific, technical, or historical information from NASA programs, projects, and missions, often concerned with subjects having substantial public interest.

- TECHNICAL TRANSLATION. English-language translations of foreign scientific and technical material pertinent to NASA's mission.

For more information about the NASA STI program, see the following:

- Access the NASA STI program home page at http://www.sti.nasa.gov

- E-mail your question to help@sti.nasa.gov

- Fax your question to the NASA STI Information Desk at 757-864-6500

- Telephone the NASA STI Information Desk at 757-864-9658

- Write to:
  NASA STI Program
  Mail Stop 148
  NASA Langley Research Center
  Hampton, VA 23681-2199

NASA/TM—2017-219703

The Effects of Fiber Orientation and Adhesives on Tensile Properties of Carbon Fiber Reinforced Polymer Matrix Composite With Embedded Nickel-Titanium Shape Memory Alloys

Derek J. Quade
Glenn Research Center, Cleveland, Ohio

Sadhan C. Jana, Gregory N. Morscher, and Manigandan Kannan
University of Akron, Akron, Ohio

Linda S. McCorkle
Ohio Aerospace Institute, Brook Park, Ohio

National Aeronautics and
Space Administration

Glenn Research Center
Cleveland, Ohio 44135

November 2017

This report is a formal draft or working paper, intended to solicit comments and ideas from a technical peer group.

This report contains preliminary findings, subject to revision as analysis proceeds.

Level of Review: This material has been technically reviewed by technical management.

Available from

NASA STI Program
Mail Stop 148
NASA Langley Research Center
Hampton, VA 23681-2199

National Technical Information Service
5285 Port Royal Road
Springfield, VA 22161
703-605-6000

This report is available in electronic form at http://www.sti.nasa.gov/ and http://ntrs.nasa.gov/

The Effects of Fiber Orientation and Adhesives on Tensile Properties of Carbon Fiber Reinforced Polymer Matrix Composite With Embedded Nickel-Titanium Shape Memory Alloys

Derek J. Quade
National Aeronautics and Space Administration
Glenn Research Center
Cleveland, Ohio 44135

Sadhan C. Jana, Gregory N. Morscher, and Manigandan Kannan
University of Akron
Akron, Ohio 44325

Linda S. McCorkle
Ohio Aerospace Institute
Brook Park, Ohio 44142

Abstract

Nickel-titanium (NiTi) shape memory alloy (SMA) sections were embedded within carbon fiber reinforced polymer matrix composite (CFRP/PMC) laminates and their tensile properties were evaluated with simultaneous monitoring of modal acoustic emissions. The test specimens were fabricated in three different layup configurations and two different thin film adhesives were applied to bond the SMA with the PMC. A trio of acoustic sensors were attached to the specimens during tensile testing to monitor the modal acoustic emission (AE) as the materials experienced mechanical failure. The values of ultimate tensile strengths, strains, and moduli were obtained. Cumulative AE energy of events and specimen failure location were determined. In conjunction, optical and scanning electron microscopy techniques were used to examine the break areas of the specimens. The analysis of AE data revealed failure locations within the specimens which were validated from the microscopic images. The placement of 90° plies in the outer ply gave the strongest acoustic signals during break as well as the cleanest break of the samples tested. Overlapping 0° ply layers surrounding the SMA was found to be the best scenario to prevent failure of the specimen itself.

1.0 Introduction

The use of shape memory alloys (SMAs) within composite materials has formed an active area of research in the past decade. The SMAs are able to generate large amounts of stress while embedded within composite structures if they are triggered by resistive heating or sensible temperature change. Initial research efforts in this area focused on characterization of NiTi wires and NiTi strips within a variety of composites during activation (Refs. 1 to 4). The dynamics of SMA activation within composite materials is an active area of research, looking at 3-point bend and beam analysis (Ref. 5), debonding mechanics during activation (Ref. 6), as well as bending and twisting in simple composites (Ref. 7) and more advanced plate composite structures (Refs. 8 and 9). Beyond basic mechanics, fabrication and implementation of NiTi chevrons has been accomplished (Ref. 10), as well as a variety of actuators utilizing polymer composite materials embedded with SMAs (Refs. 11 to 13). All the aforementioned research is possible due to the functional property of the SMA based on the reversible, thermoelastic martensitic transition of the crystalline structure (Ref. 14). Austenitic crystals shift to a variety of martensitic configurations at the times of heating or loading and unloading. This shift in configuration is

directly responsible for the generation of stresses within the materials when they are constrained in the composites (Ref. 15). The flexibility and stiffness of an actuator can be optimized by using different layups within the composites, in relation to the placement of the SMAs in composite panels.

Prior research work focused on areas such as modeling the stresses within the PMC (Refs. 10 to 12), enhancing the bond between SMA and the host composite (Refs. 6, 7, and 16), and full scale application of the resultant SMA-PMC actuators (Refs. 11 to 13). In all cases, the interactions and optimization of the bonds between SMA and composite received significant attention (Refs. 1 to 16). A majority of experimental systems capitalized on optically clear systems, such as transparent glass (Ref. 3) or aramid fibers (Refs. 1, 2, 7, and 10) paired with optically clear resins. Optical methods, such as Raman spectroscopy, were used for monitoring of stress and debonding at the interfaces of two dissimilar materials (Refs. 1, 4, 7, 10, and 15). Exceptions are carbon fiber reinforced polymers – CFRP's where the interactions between SMA's and PMC's could not be monitored with the above methods (Refs. 16 and 17) due to opacity of the composite panels. As is evident, the research in this narrow area has focused primarily on the interactions and processing of the SMA and CFRP with little to no focus on the effects of CFRP structure on how the SMA would respond under thermal trigger.

The goal of the present research is to examine the effects of bonding between the SMA and the PMC in the composite panels in the presence of an adhesive. In conjunction, the work focuses on how the structure of the CFRP influences the interfacial bond between SMA and PMC. For this purpose, three composite specimens with the same weight ratio of SMA and PMC but differing ply configurations were tested under tension. These configurations alternated 9 plies of ±45°, 0°, and 90° fiber directions with the 0° ply orientation in line with the load direction, and 90° ply orientated perpendicular to the direction of the load. Two film adhesives were used to bond the SMA to the interior of the PMC. A control bond of the default PMC epoxy phase was tested as well. Mechanical tests were performed in accordance to the ASTM D3039 method, the standard test method for tensile properties of polymer matrix composite materials (Ref. 18). A trio of acoustic sensors were attached to the specimens to monitor the modal acoustic emissions (MAE) during failure. The MAE was used to see if an optimal layup configuration exists within the PMC for crack/debonding monitoring of the SMA-PMC bond when failure occurs.

2.0 Experimental Techniques

2.1 Adhesive Bonding Scenarios

Three adhesive bonding scenarios were pursued in this study. As control, no adhesive was used in promoting bonding between the NiTi section and the epoxy matrix of the PMC. In this case, the epoxy phase of the composite produced adhesion at the metal-polymer interfaces.

2.2 Layup Scenarios

In conjunction with the use of two different adhesives, three different CFRP layups were used to produce the final composite materials. To conform to the thicknesses required by the ASTM D3039 method (Ref. 18), a 9-ply CFRP with a thickness of 1.5 mm was used. The first PMC layup consisted of a (+45/0/-45/90/0/90/-45/0/+45) orientation of the plies, the second consisted of a (+45/90/-45/0^3/ -45/90/+45) orientation, and the third consisted of a (90/+45/0/-45/0/-45/0/+45/90) orientation. In each case, a set of composites was prepared by inserting the SMAs into the midplane. These configurations are shown in Figure 1.

The initial layup scenarios consisted of 8-ply configurations with SMA's embedded in the center; these layups resulted in SMA "bumps" within the specimens after composite fabrication. In view of this, a central 0° ply with embedded SMA was applied, resulting in a smooth specimen.

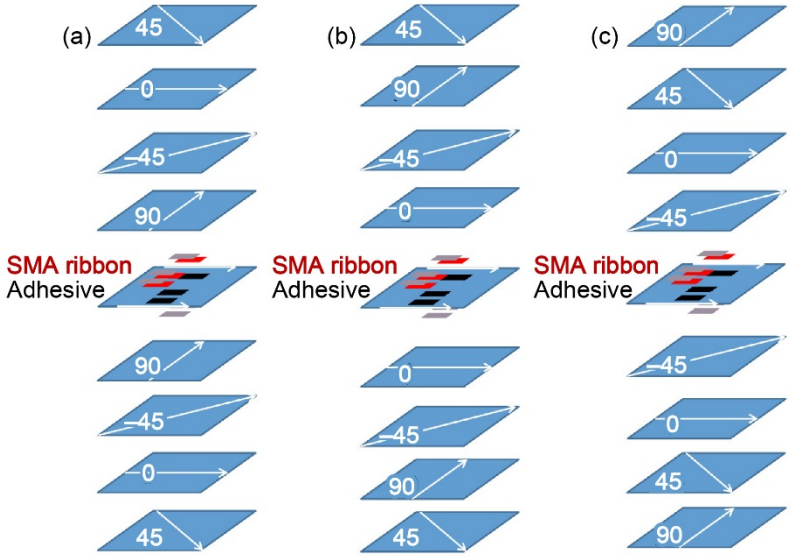

Figure 1.—Specimen layup configuration for tensile tests. (a) Layup 1: (+45/0/-45/90/0/90/-45/0/+45), (b) Layup 2: (+45/90/-45/0/0/0/ -45/90/+45), (c) Layup 3: (90/+45/0/-45/0/-45/0/+45/90).

2.3 Materials and Fabrication

Flat annealed NiTi sheets were supplied by Johnson Matthey (San Jose, California), measuring 457.2 mm in length, 101.6 mm in width, and 0.127 mm in thickness. Rectangular strips were cut from these sheets of length 25.4 mm and width 0.127 mm, cleaned with acetone, and dried. The PMC used was a HexPly 8552 Epoxy Matrix embedded with IM7 carbon fibers obtained from Hexcel (Salt Lake City, Utah) (Ref. 19). For control specimens, no adhesive was placed between the NiTi section and the PMC. The rest of the samples were bonded using the film adhesives Hysol EA9696 (Ref. 20) (Bay Point, California) and Cytec FM 377U (Ref. 21) (Olean, New York).

Specimens were assembled as 152.4 by 152.4 mm panels according to the layup guidelines shown in Figure 1. The control specimens with no SMA were cured with the panels that contained SMA so as to minimize the variability of specimen preparation. This configuration is shown in Figure 2.

Once each panel was assembled, they were placed in an autoclave and cured following a procedure specified for HexPly 8552 (Ref. 19). Specifically, the parts were first cured for 1 hr at 110 °C under full vacuum and a pressure of 0.1 MPa. Then the temperature was ramped up to 176 °C and vacuum vented when the pressure increased beyond 0.2 MPa to a total pressure of 0.68 MPa for 2 hr. In each case, three control specimens with no SMA and three specimens with SMA were prepared. Additional panels were fabricated to make sure that a minimum count of five specimens was available for each series, as mandated by the ASTM D3039 method (Ref. 18). Specimens were then cut via water jet into 25.4 mm wide, 152.4 mm long parts for tensile testing, as schematically shown in Figure 2. After cutting, specimens were c-scanned to detect any debond at the cut areas. Specimens without edge defects were then tabbed with E-glass materials attached via AF 163-2M film adhesive (Ref. 22). Tabs were 25.4 by 25.4 mm in size, attached to the designated “grip” sections seen in Figure 3.

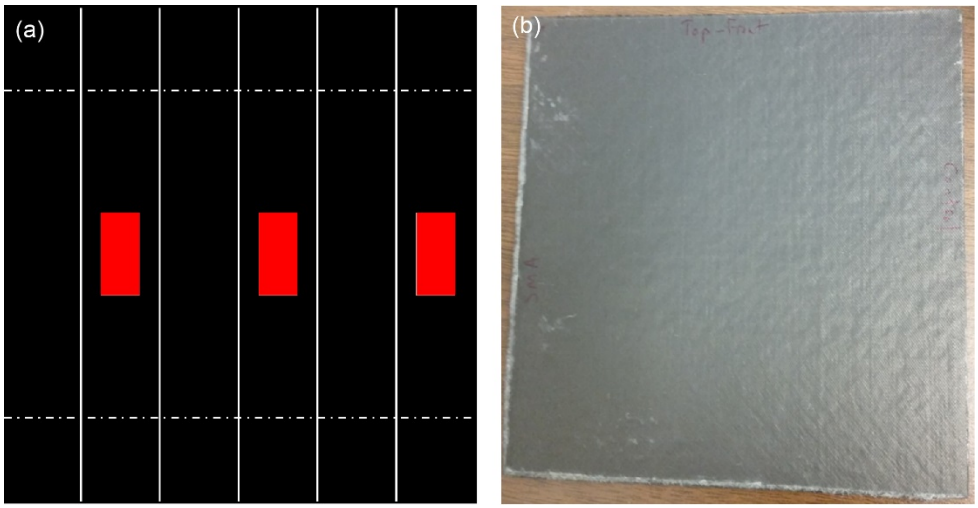

Figure 2.—(a) Schematic of 152.4 by 152.4 mm panel configuration—PMC in black, SMA in red; (b) Actual panel.

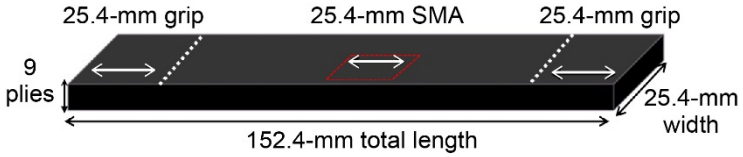

Figure 3.—Final specimen dimensions for tensile testing.

2.4 Tensile Testing

All specimens were subjected to tensile elongation according to ASTM D3039 method. E-glass tabs were used to grip the specimens in an Instron 5582 tensile testing device running the Bluehill V 2.0 software suite. Three acoustic sensors were attached to the specimens at the center, 25.4 mm above, and 25.4 mm below the center line. Vacuum grease was used to secure solid body contact of the sensor with the test specimen. In addition, clips were used to secure the sensors to the specimen. The acoustic sensors were connected to a Digital Wave preamplifier, which in turn was connected to a computer running the WaveExplorer software suite (Digital Wave, Huntingdon Valley, PA). AE sampling was performed at a rate of 10 MHz, while 2048 data points for each waveform was recorded, including 512 per-trigger points. The correct placement of the AE sensors and the functioning of the sensors were checked by performing lead break tests. Samples were pulled apart at a constant rate of 1.27 mm/min until the specimen failed. Figure 4 shows a test specimen with attached AE sensors.

Optical microscopy was performed on an Olympus Microscope DFC295 utilizing the Leica Applications Suite Software. Specimen break patterns were similar throughout testing, with the most important factor being the orientation of the carbon fibers. These similarities are shown for control specimens A, B, and C. Images in Figure 5 show the break plane, edge, and inner ply cracking of specimen A-2. The images shown in Figure 5 highlight the break area that occurred during tensile testing. Mild breaks occurred unevenly throughout the different orientations of the inner plies, while edge cracking showed the extent of intra-laminar cracking that occurred at points traversing away from the actual break area.

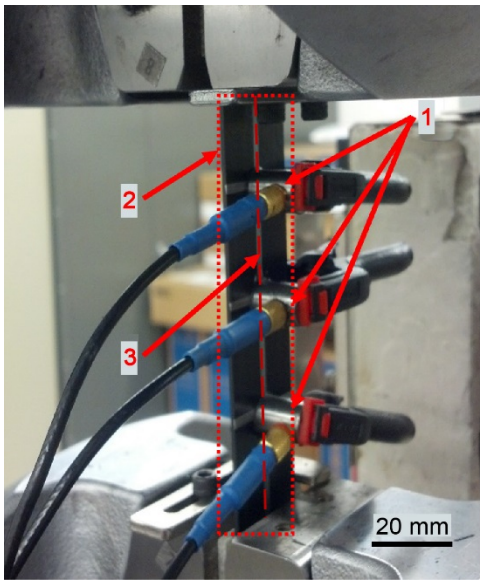

Figure 4.—Three acoustic sensors (1) mounted on tensile specimen (2) along center line (3).

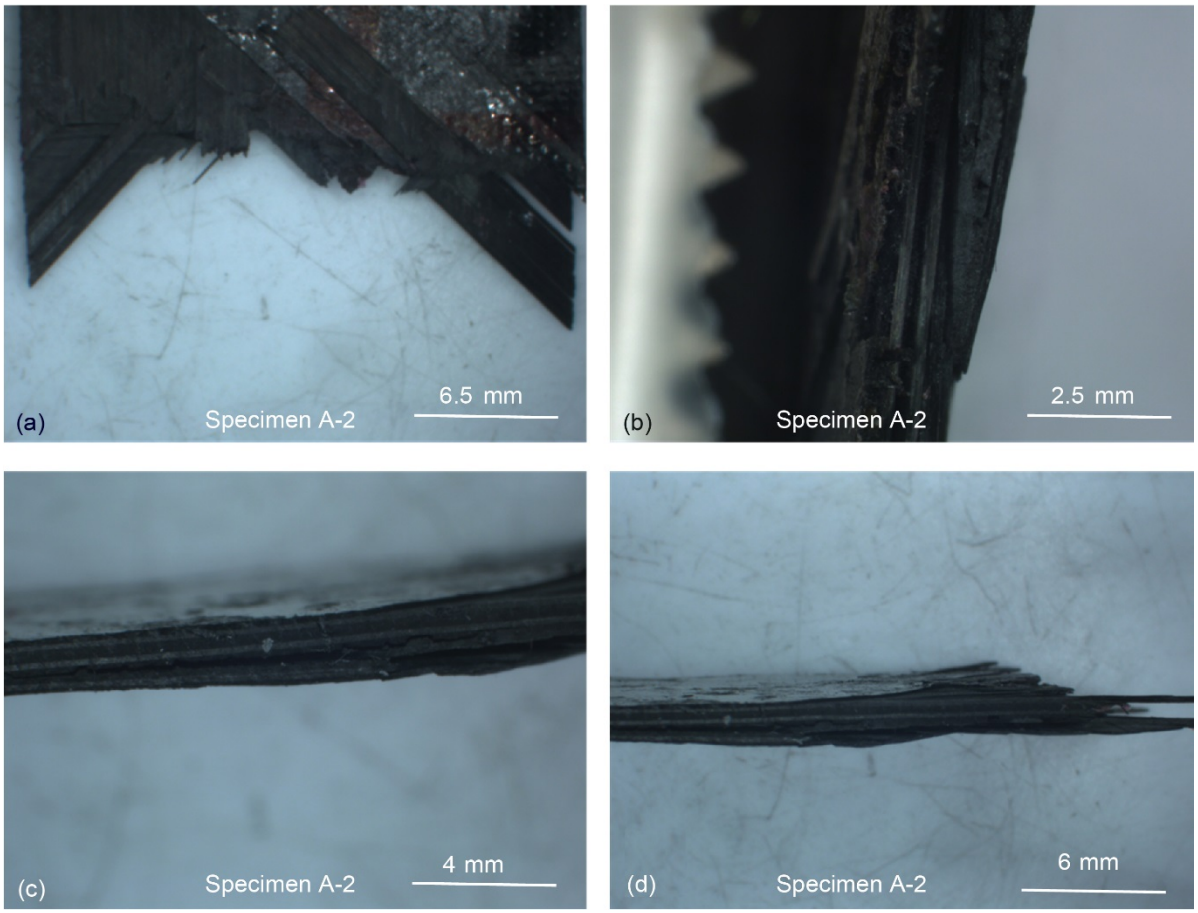

Figure 5.—Optical microscopy of specimen A-2. (a) Break edge, (b) Inner plies, (c) and (d) Crack edges.

Figure 6 highlights the break area, edge, and inner ply cracking for specimen B-2. In these images, much more explosive break is shown. Compared to Figure 5, more extensive inner fiber damage can be seen for the layup used for specimen B-2. A higher amount of intra-laminar cracking traversing away from the actual point of break is seen as well. These cracks do not penetrate the inner layers of the B-2 composite, however, as shown in Figure 6(c).

Figure 7 highlights the break area, edge, and inner ply cracking for specimen C-1. These images show a clean break through the specimen due to the ply layup. Fiber breaks throughout the ply layers are minimal, as seen in Figure 7(a) and (b). Intra-laminar cracking was still present throughout the specimen traversing away from the actual break point, seen in Figure 7(c) and (d).

Scanning electron microscopy was performed on a Hitachi S-4700 electron microscope running at 6 kV voltage and average working distance of 12 mm from the detector. Images were taken at the edges of the crack areas as well as on the surface of crack areas in order to highlight crack propagation at the break of the specimen (fracture) and during crack propagation along the edges (delamination).

Figure 8 and Figure 9 present SEM images of the specimen A-4 taken along the edge crack delamination area and surface crack fracture area, respectively.

Figure 10 and Figure 11 show representative SEM images of specimen B-4 taken along the edge crack delamination area and the surface crack fracture area, respectively.

Figure 12 and Figure 13 show the SEM images of specimen C-4 taken along the edge crack delamination area and the surface crack fracture area, respectively.

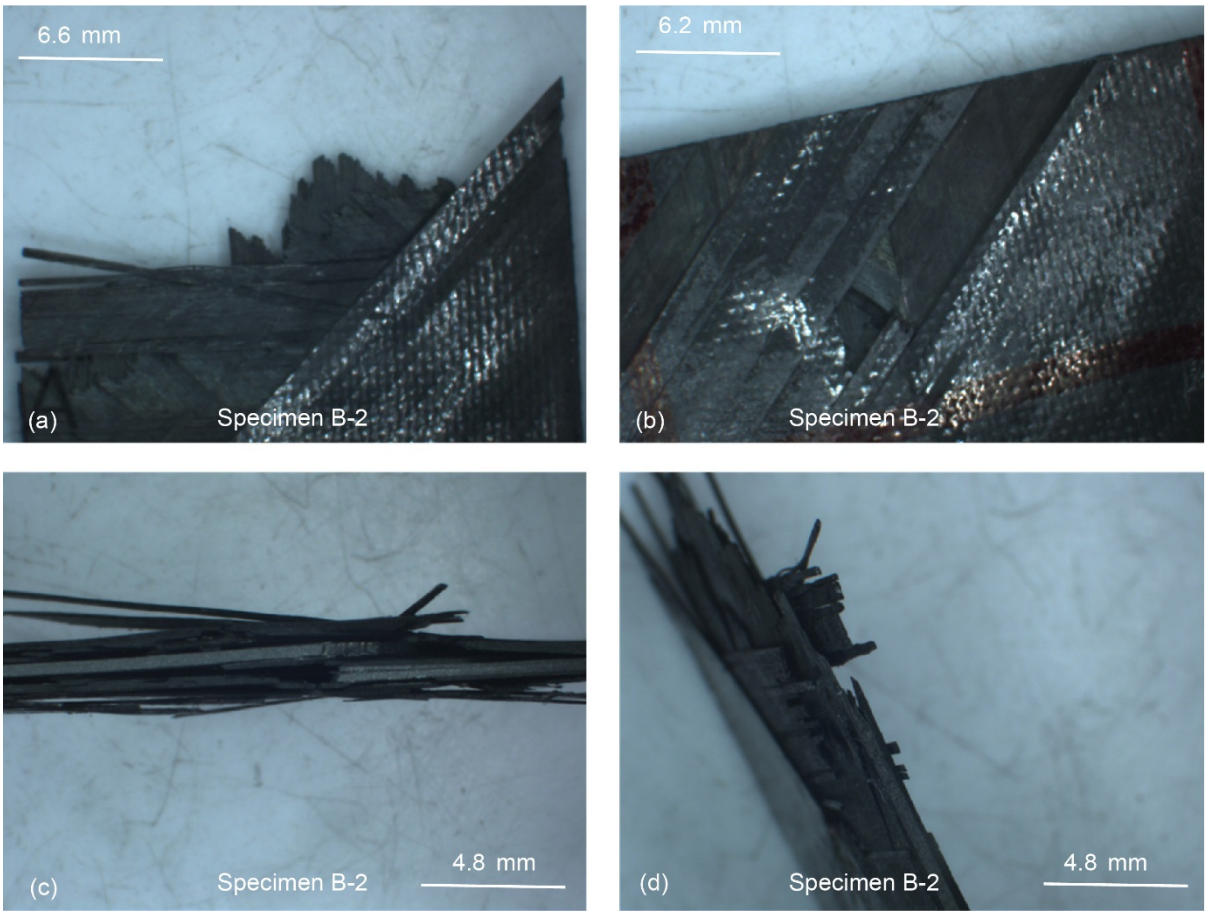

Figure 6.—Optical microscopy of specimen B-2. (a)/(b): Break edge, (c)/(d): Crack edges.

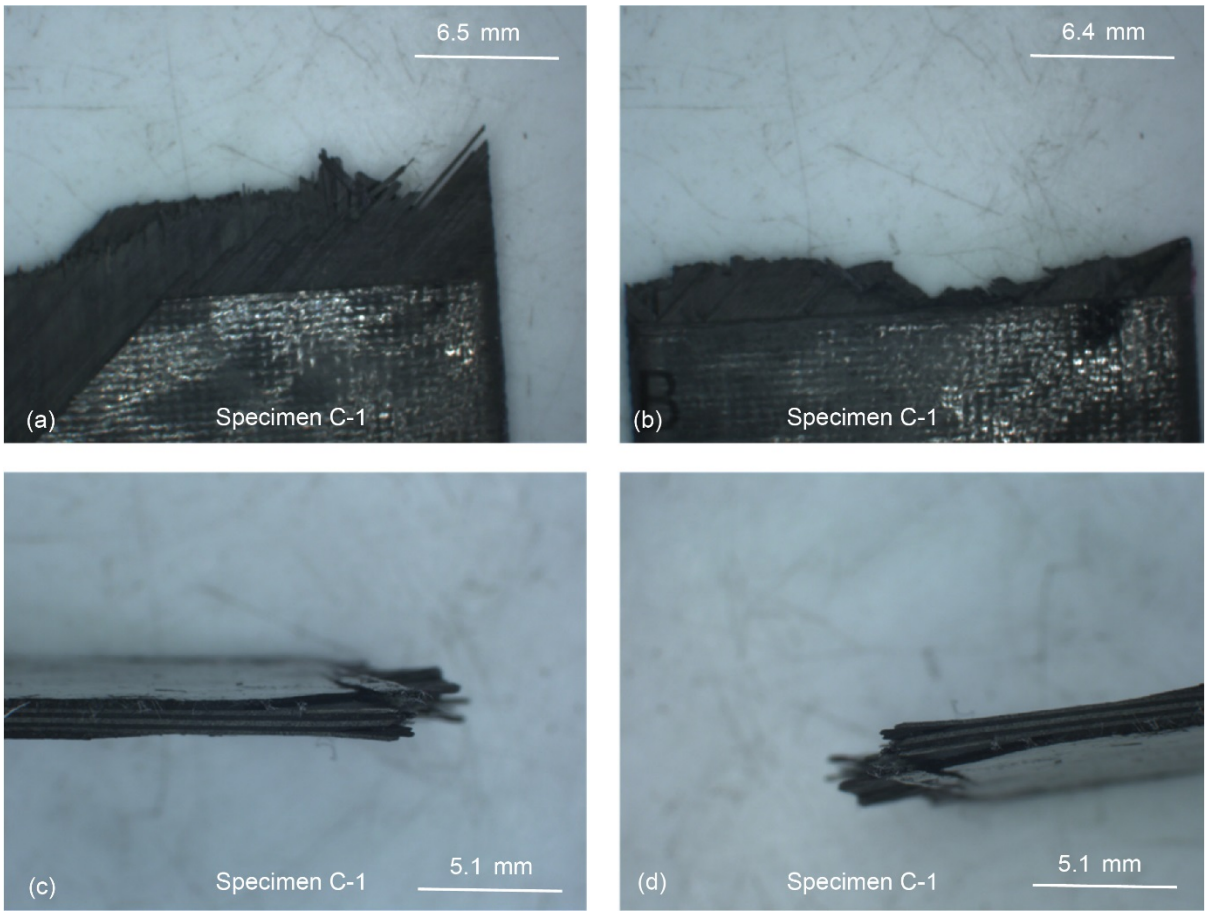

Figure 7.—Optical microscope images of specimen C-1. (a)/(b) Break edge, (c)/(d): crack edges.

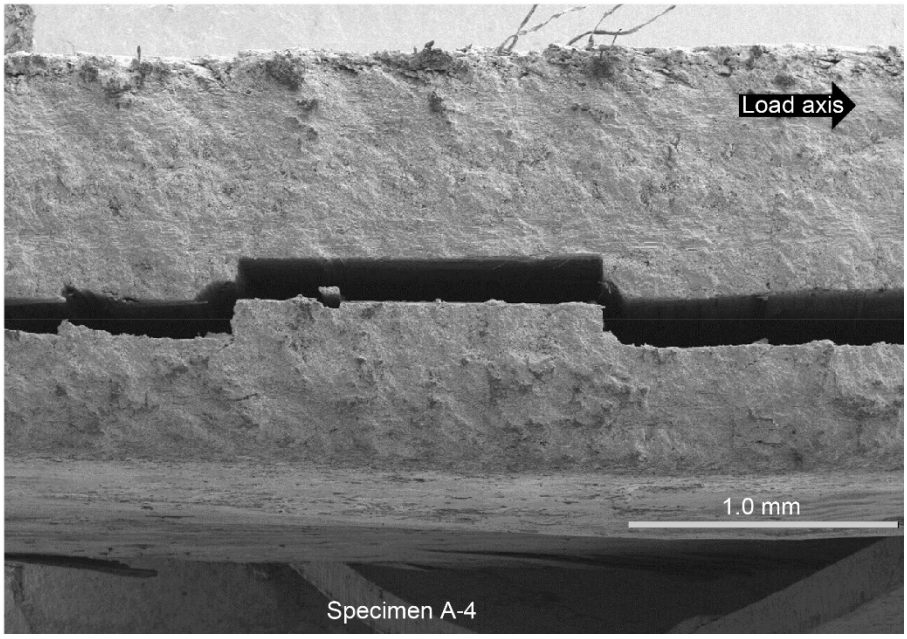

Figure 8.—SEM image of edge crack delamination of specimen A-4.

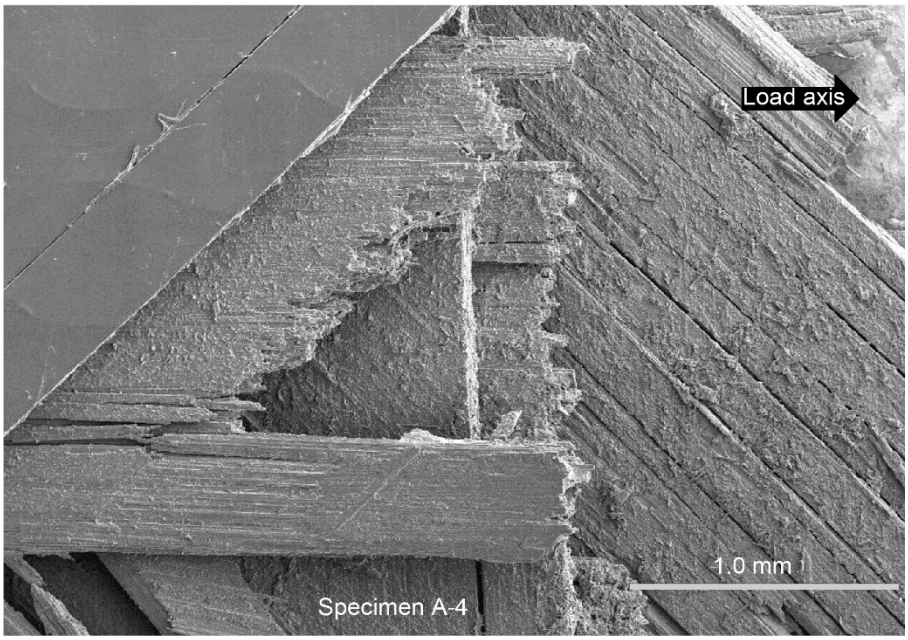

Figure 9.—SEM image of surface crack fracture of specimen A-4.

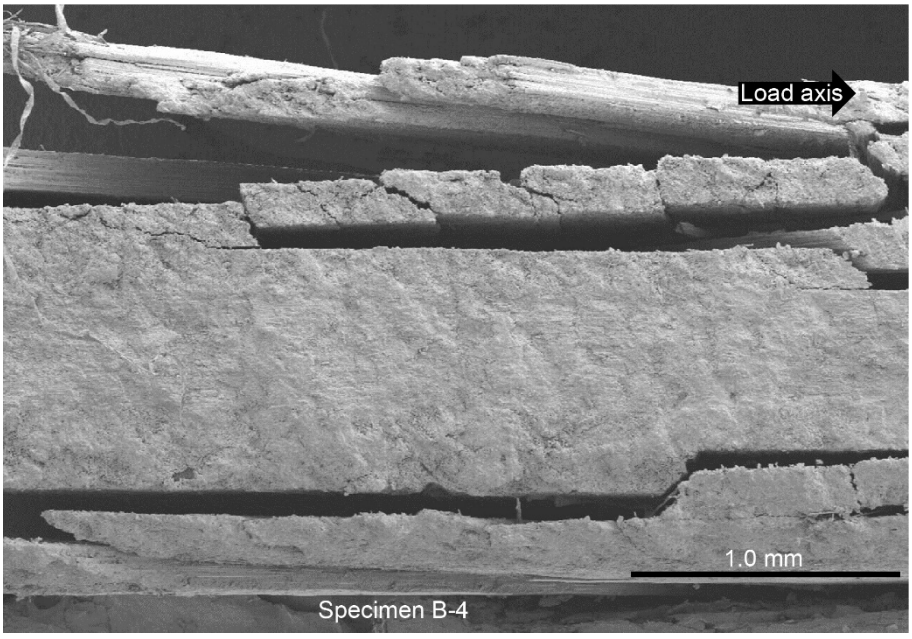

Figure 10.—SEM image of edge crack delamination of specimen B-4.

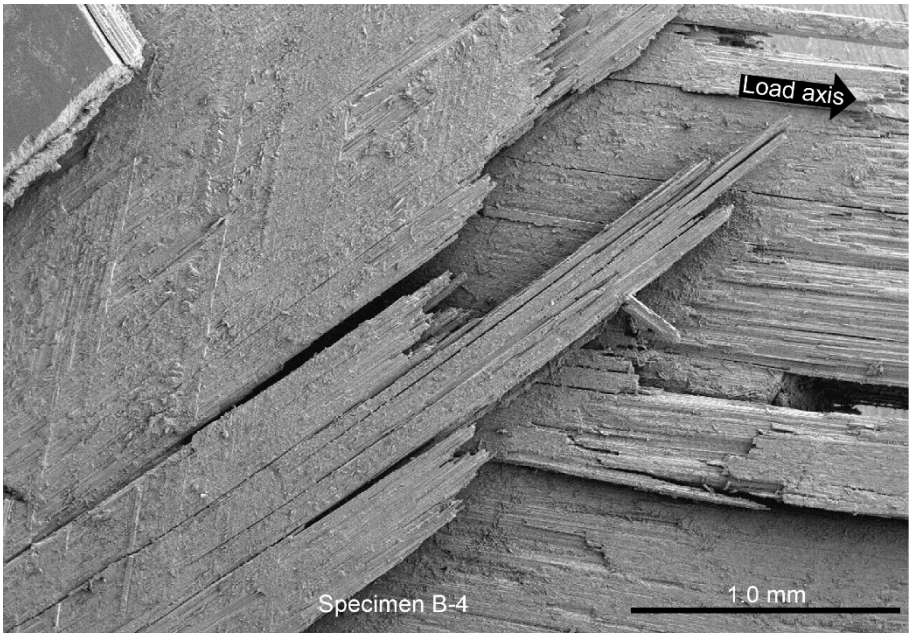

Figure 11.—SEM image of surface crack fracture of specimen B-4.

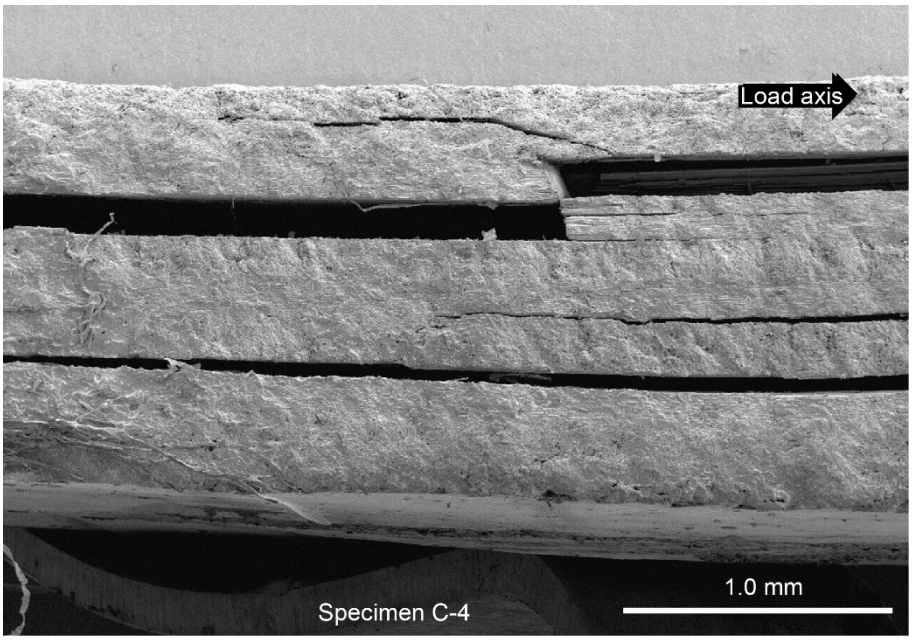

Figure 12.—SEM image of edge crack delamination of specimen C-4.

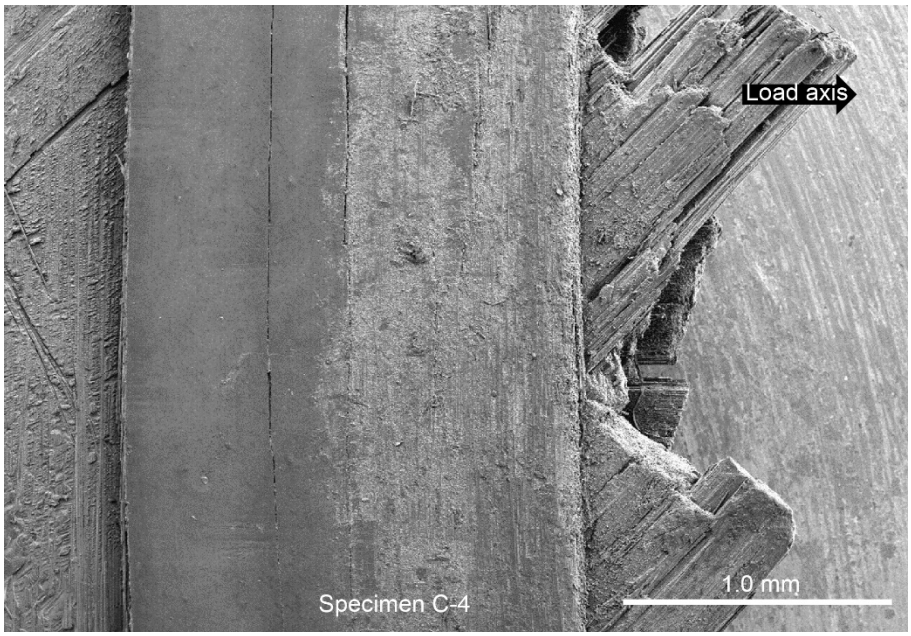

Figure 13.—SEM image of surface crack fracture of specimen C-4.

3.0 Results

3.1 Tensile Test Data

Table 1 shows all of the tested samples. Samples A-C consisted of control samples, i.e., without SMA, samples D-F consisted of SMA samples without the adhesives, samples G-I represent specimens with SMA bonded with Hysol EA9696 adhesive, and samples J-L represent SMA samples bonded with FM 377U adhesive. Figure 14 shows the stress vs. strain curves of the A-series specimens.

3.2 Acoustic Emission Data

As presented earlier, a trio of acoustic sensors were attached to each specimen before subjecting them to tensile tests. As the specimens underwent failure, acoustic events were recorded and marked at each time instant. The cumulative AE energy of events are plotted alongside stress for each of the test specimens to better correlate the acoustic signal with the mechanical failure events. A representative graph of this data is shown in Figure 15.

Acoustic signals detected can be directly attributed to breaks and cracking within the specimen during testing. Figure 15 highlights both the start and extent of internal cracking within specimen B-1 at distinct times. Specimen micro-cracking begins at a test time of ~115 s, when AE signals are first detected. As the test proceeds, large energy signatures throughout the specimen are noted to occur at ~190 s, with the final failure sequence starting around ~210 s and ending at ~260 s.

TABLE 1.—TESTED SAMPLES

Control Layup 1	Control Layup 2	Control Layup 3	SMA No Adh Layup 1	SMA No Adh Layup 2	SMA No Adh Layup 3	SMA Hysol Layup 1	SMA Hysol Layup 2	SMA Hysol Layup 3	SMA FM Layup 1	SMA FM Layup 2	SMA FM Layup 3
A-1	B-1	C-1	D-1	E-1	F-1	G-1	H-1	I-1	J-1	K-1	L-1
A-2	B-2	C-2	D-2	E-2	F-2	G-2	H-2	I-2	J-2	K-2	L-2
A-3	B-3	C-3	D-3	E-3	F-3	G-3	H-3	I-3	J-3	K-3	L-3
A-4	B-4	C-4	D-4	E-4	F-4	G-4	H-4	I-4	J-4	K-4	L-4
A-5	B-5	C-5	D-5	E-5	F-5	G-5	H-5	I-5	J-5	K-5	L-5
A-6	B-6	C-6	D-6	E-6	F-6	G-6	H-6	I-6	J-6	K-6	L-6

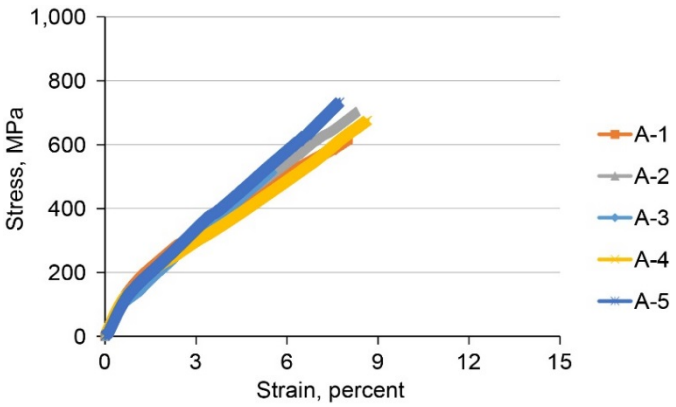

Figure 14.—Stress-strain graph for control series A.

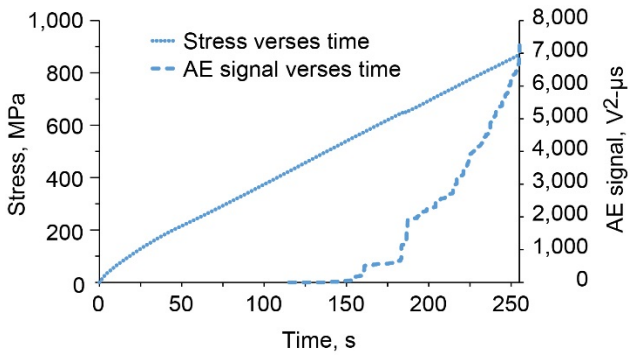

Figure 15.—Cumulative AE energy of events and stress plotted against time for specimen B-1.

4.0 Analysis

A numerical analysis was performed of the results obtained from tensile testing, as well as AE taken at different locations. Mechanical analysis was based on equations presented by ASTM Standard D3039 (Ref. 18). These results highlight the differences in bonding between SMA and the PMC in tensile tests, as well as the acoustic failure of the specimens.

4.1 Analysis of Tensile Test Results

The ultimate tensile strength values were calculated for each specimen using Equations (1) and (2):

$$F^{tu} = {P^{max}}/{A} \tag{1}$$

$$\sigma_i = {P_i}/{A} \tag{2}$$

In Equations (1) and (2), F^{tu} is the ultimate tensile strength (MPa), P^{max} is the maximum force before failure (N), σ_i is the tensile stress at the *i*-th data point (MPa), P_i is the force at the *i*-th data point (N), and A is the average cross-sectional area (mm^2).

The averages for each series are summarized in Figure 16 for comparative analysis.

The values of engineering strain and the ultimate strain were calculated using Equation (3):

$$\varepsilon_i = {\delta_i}/{L_g} \tag{3}$$

where ε_i is the tensile strain at the *i*-th data point (ε), δ_i is the machine displacement at *i*-th data point (mm), and L_g is the specimen gage length (mm).

The average values of ultimate tensile strain for various specimen are summarized in Figure 17.

The chord modulus of elasticity was calculated using Equation (4) as follows:

$$E^{chord} = {\Delta\sigma}/{\Delta\varepsilon} \tag{4}$$

where E^{chord} is the tensile chord modulus of elasticity (GPa), $\Delta\sigma$ is the difference in applied tensile stress between two strain points (MPa), and $\Delta\varepsilon$ is the difference between two strain points (nominally 0.002). Chord moduli values were calculated at the initial linear region of the stress-strain curves.

The average values of chord modulus for each series are summarized in Figure 18.

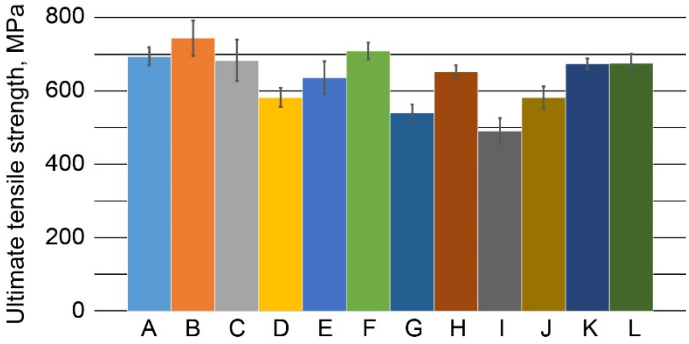

Figure 16.—Ultimate tensile strength of various specimens. A-C: Control, D-F: SMA control, G-I: SMA with Hysol adhesive, J-L: SMA with FM adhesive.

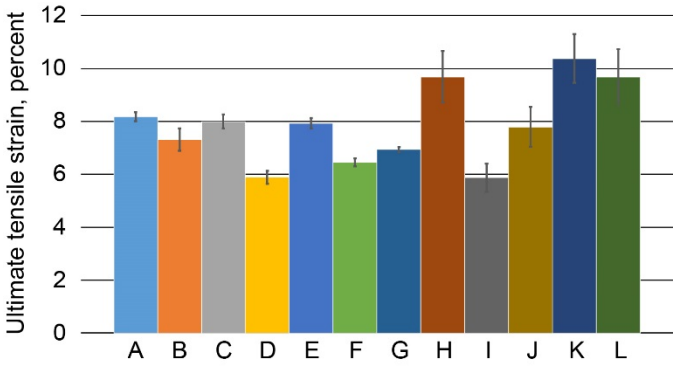

Figure 17.—Ultimate engineering tensile strain averages for tensile testing. A-C: Control, D-F: SMA control, G-I: SMA with Hysol adhesive, J-L: SMA with FM adhesive.

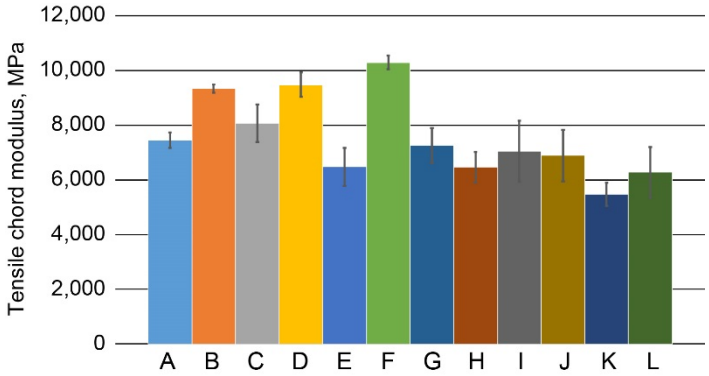

Figure 18.—Tensile chord moduli averages for tensile testing. A-C: Control, D-F: SMA control, G-I: SMA with Hysol adhesive, J-L: SMA with FM adhesive.

4.2 Analysis of Data From Acoustic Emission

In prior work (Refs. 23 to 26), analysis of composite materials via AE centered on peak frequency analysis of the waveforms generated. However, the results reported in earlier work led to different conclusions on the types of damages occurring at different frequency values. For this reason, a more simplified analysis of AE data is presented in this paper. Modal Acoustic Emissions (MAE) was utilized in order to examine the two dominant modes in tensile failure of thin plates. These are high frequency wavelengths in extensional mode and lowest order anti-symmetric waves in flexural mode. One of the strongest applications of MAE is the ability to locate the sources of an acoustic wave based upon when that acoustic wave is detected by a sensor.

4.2.1 Modal AE Location

The analysis of AE data is based on a set of equations developed by Morscher (Ref. 27). These equations were developed in order to track the crack locations within tensile specimens based on acoustic measurements generated during failure. One such equation is presented below:

$$\text{Location} = \frac{x}{2} * \left(\Delta t / \Delta t_x\right) \tag{5}$$

where x is the distance between the two outer AE sensors, Δt is the arrival time of sensor A subtracted by the arrival time of sensor C (microseconds), and Δt_x is the outer position arrival time of sensor A subtracted by the arrival time of sensor C (microseconds).

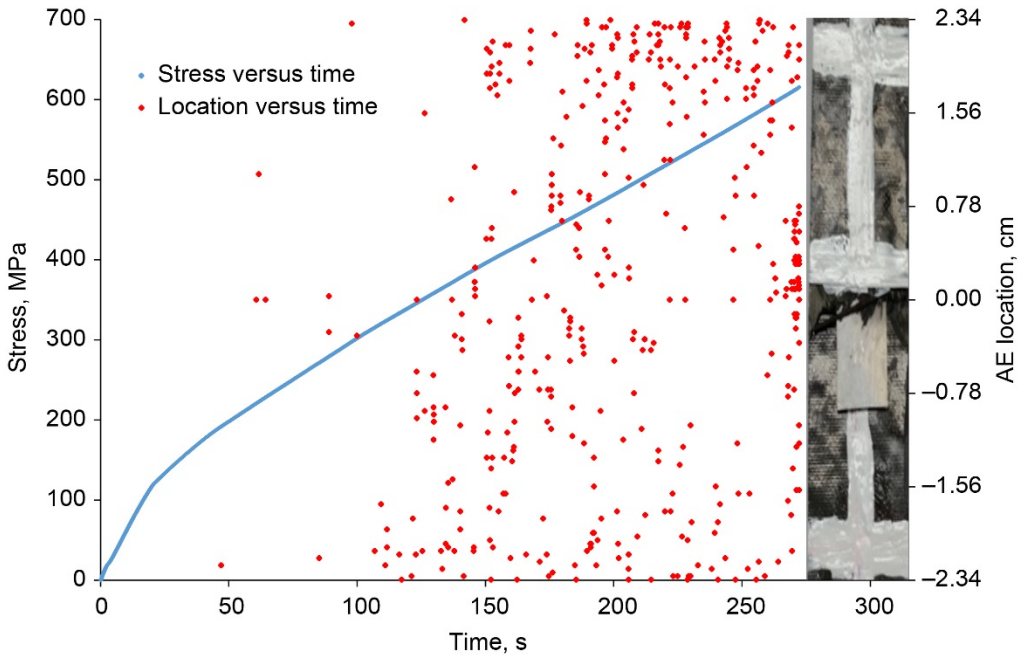

Figure 19.—Stress and AE location plotted against time for specimen L-1.

Recall that sensors A and C are the upper and lower most sensors on the specimen. The Wave Explorer software allows tracking of the specific times when the AE signals cross a particular sensor producing the values of Δt. In this regard, Δtx is the change in time between the outer sensors when an acoustic event takes place far *outside* the sensor locations. This is achieved during lead breaks, where an extensional wave, generated by the breaking of pencil lead on the sample is produced far outside the sensor locations. Using Equation (5), AE events between sensors A and C can be accurately located.

Figure 19 shows a plot of stress versus time and acoustic signals generated during tensile testing. The AE signals shown in this graph, however, correlate to specific two-dimensional locations on the specimen itself. For better reference, an image of the broken specimen (between sensor A and C) is placed alongside the graphs.

Placement of the specimen image alongside the graph helps give definitive locations for cracks during tensile failure. These locations can also be correlated to the time as well as the stress present within the specimen when the acoustic energy from cracking was produced. Clusters of acoustic signals at part failure match where ultimate failure of the specimen occurred.

Along with the location plots shown above, stress versus AE energy plots, inspired by Baker (Ref. 28), were generated. In these plots, the stress is directly plotted against the cumulative AE energy of events. By manipulating the AE time data to match with specific time points of stress, the time axis seen in Figure 19 can be removed, allowing a direct comparison of stress and acoustic energy. An example of the trend is shown in Figure 20.

The trends in the above figure directly correlate the stress present in a tested system to the amount of acoustic energy recorded. This relationship is directly connected to the layup of the system. In Figure 20, the A series layup generates significantly less acoustic energy in comparison to other layups. The highest amount of acoustic energy generated during tensile testing is seen for the layup in the C series.

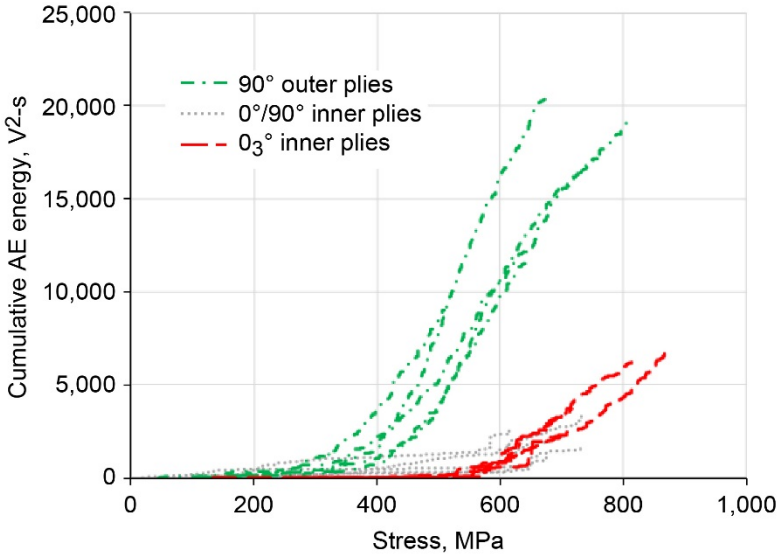

Figure 20.—Stress vs. cumulative AE energy for tensile control series—blue for layup 1, red for layup 2, green for layup 3.

5.0 Discussion

5.1 Simplified Composite Analysis

The strength and stiffness of a composite depends on the orientation sequences of the plies (Ref. 29). The range of strength and stiffness of CFRP fall between the low values of fiberglass and the high values of titanium (Ref. 29). The range of these values is determined as function of the orientation of the plies to the applied load. A part designed with 0° plies reacts best to the axial tensile loads while ±45 plies react best to shear loads. A specimen with 90° plies reacts best to the side loads. This is due to the fact that in a composite part, the fiber is the load carrying element; a composite material is only strong and stiff in the direction of the fibers. The matrix supports these fibers and bonds them together within the composite. It stands to reason that failure in a quasi-isotropic layup, as was used in this study, would first occur in the ply layers made up of fibers in the 90° orientation. This will later be shown to be true via analysis of microscopy, break patterns, and acoustic emissions strength and amount.

In this context, the placement of 90° plies dictates many properties, such as mechanical and acoustic, throughout the tested specimens. These properties include how violent the break was during failure, the tensile properties, the level of acoustic energy generated during failure, and the number of acoustic data points generated throughout testing.

5.2 Specimen Break Patterns

The break patterns seen in failed parts are as important as the tensile test data. A large fraction of composites research involves recognizing the break patterns during a variety of mechanical tests (Refs. 30 to 33). The success of repair of composites and composite hybrid structures depends on the success of selection of right materials, as well as consideration of the orientation of the repair patches similar or identical to the orientation of the part being repaired (Ref. 34).

5.2.1 Microscopy Analysis

Images of break patterns and fiber orientations are presented in Figure 21 to Figure 26. These figures show the macroscopic photograph overlaid on an SEM image and identify the plies within the SEM image. Figure 21 and Figure 22 represent the break patterns that occurred within the first layup series (+45/0/-45/90/0/90/-45/0/+45).

Figure 21 shows that delamination occurred between the lower 90° ply and –45° plies with little to no delamination seen elsewhere. Figure 22 shows the variety of breaks along the many different plies; the 90° ply underwent a clear break throughout the material. This emphasizes the importance of the 90° ply in fracture and delamination; the fracture occurred at the 90° ply first, and resulted in a delamination of the composite specimen. Figure 23 and Figure 24 present the break patterns that occurred within the second layup series (+45/90/-45/0/0/0/-45/90/+45).

Figure 23 highlights the importance of placement of the 90° plies; delamination in this image runs between the ply layers in contact with the 90° plies. Further analysis shows the lack of delamination or cracks along the central triple 0° ply. This observation gives rise to the notion that an SMA insert embedded within this area would be least likely to cause an external failure at a 90° ply. A lack of visible plies within Figure 24 highlights the fact that a break within the specimen will occur at a 90° ply and travel through the specimen as a delamination until the ultimate failure occurs within the midsection triple 0° plies.

Figure 25 and Figure 26 look at the break patterns that occurred within the third layup series (90/+45/0/-45/0/-45/0/+45/90).

Figure 25 highlights the random nature of delamination when the break of the specimen occurs all in one area. Unlike the other specimens, delamination within the third layup series varies along several of the different plies. Figure 26 highlights the “clean” break seen in this series; the break begins at the outer ply (90°) and travels quickly through the specimen. It is hypothesized that as the near instantaneous break occurs at this singular area, a variety of delamination also occur through the specimen. These delaminations vary in the ply layers that they occur within, but are smaller in comparison to the delaminations seen in layups 1 and 2, as shown in Figure 23 to Figure 26. The third layup proves to be a poor use for SMA implementation, as the random delaminations throughout the specimen occur at the very center, as well as outer plies.

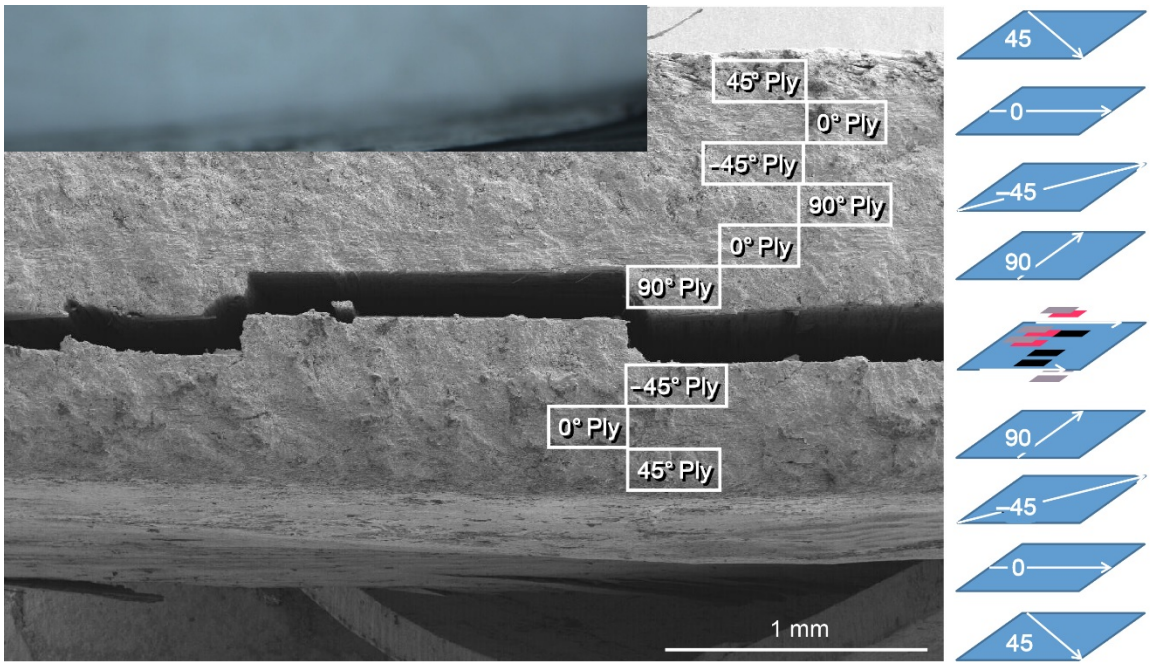

Figure 21.—Analysis of ply delamination pattern in layup 1—(+45/0/-45/90/0/90/-45/0/+45).

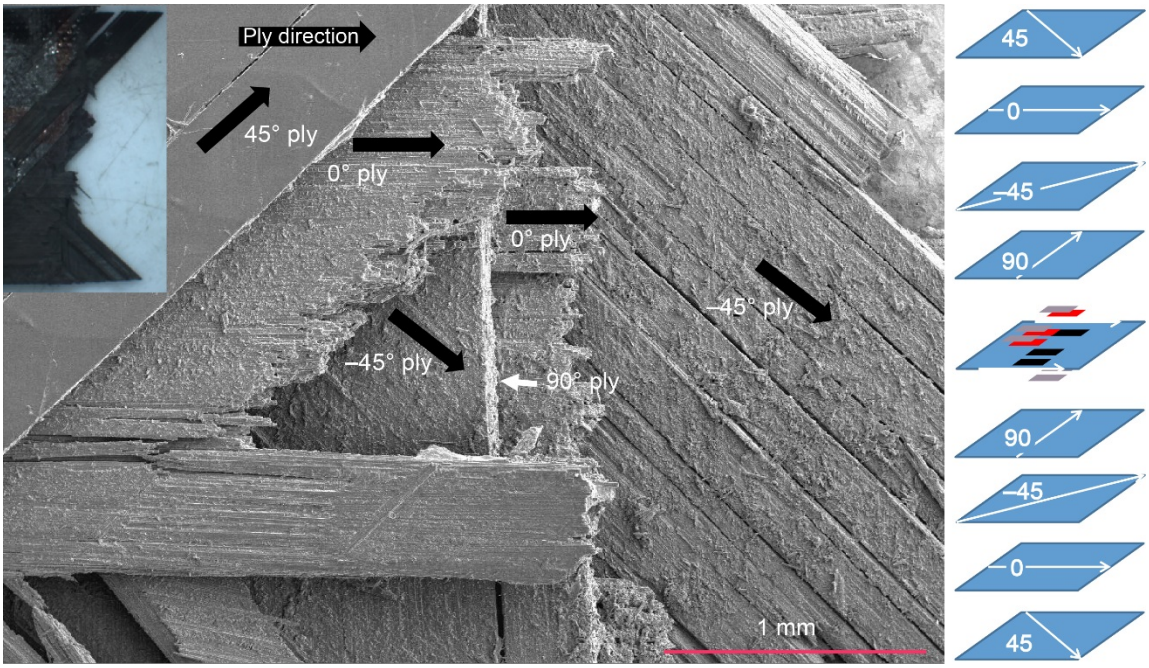

Figure 22.—Analysis of ply fracture pattern in layup 1—(+45/0/-45/90/0/90/-45/0/+45).

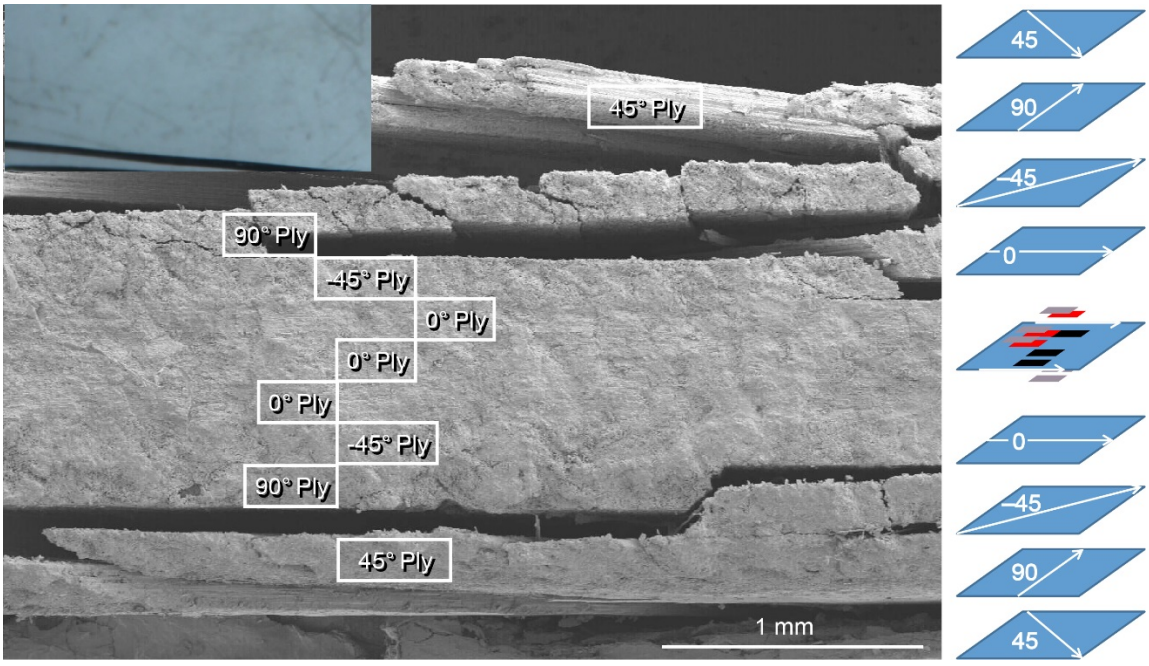

Figure 23.—Analysis of ply delamination pattern in layup 2—(+45/90/-45/0/0/0/-45/90/+45).

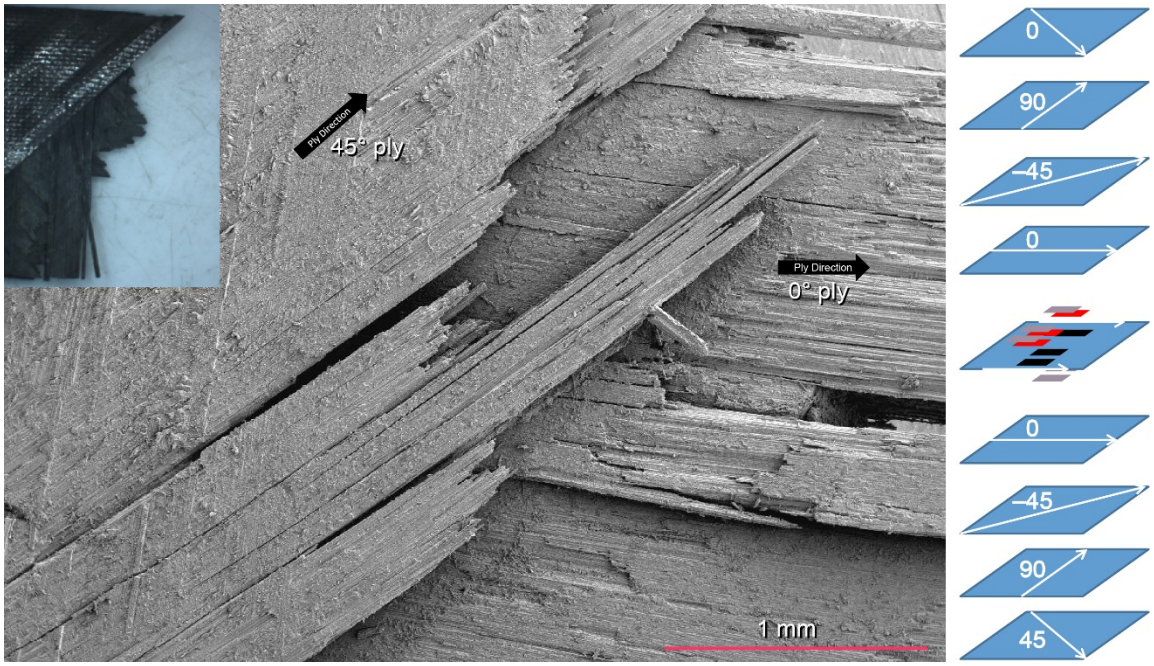

Figure 24.—Analysis of ply fracture pattern in layup 2—(+45/90/-45/0/0/0/-45/90/+45).

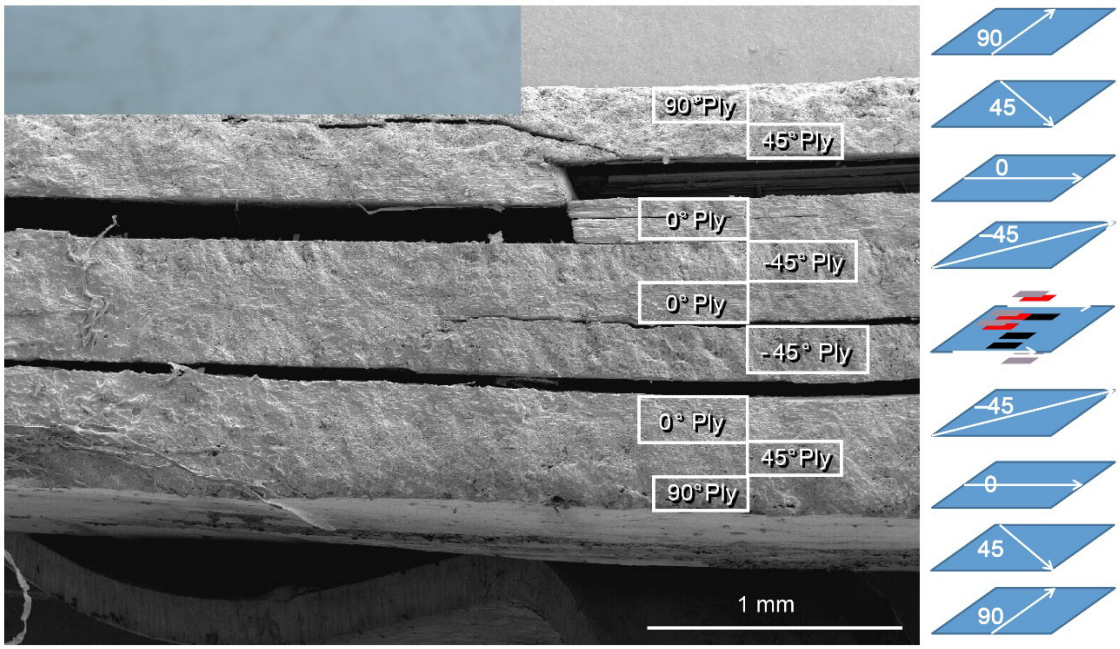

Figure 25.—Analysis of ply delamination pattern in layup 3—(90/+45/0/-45/0/-45/0/+45/90).

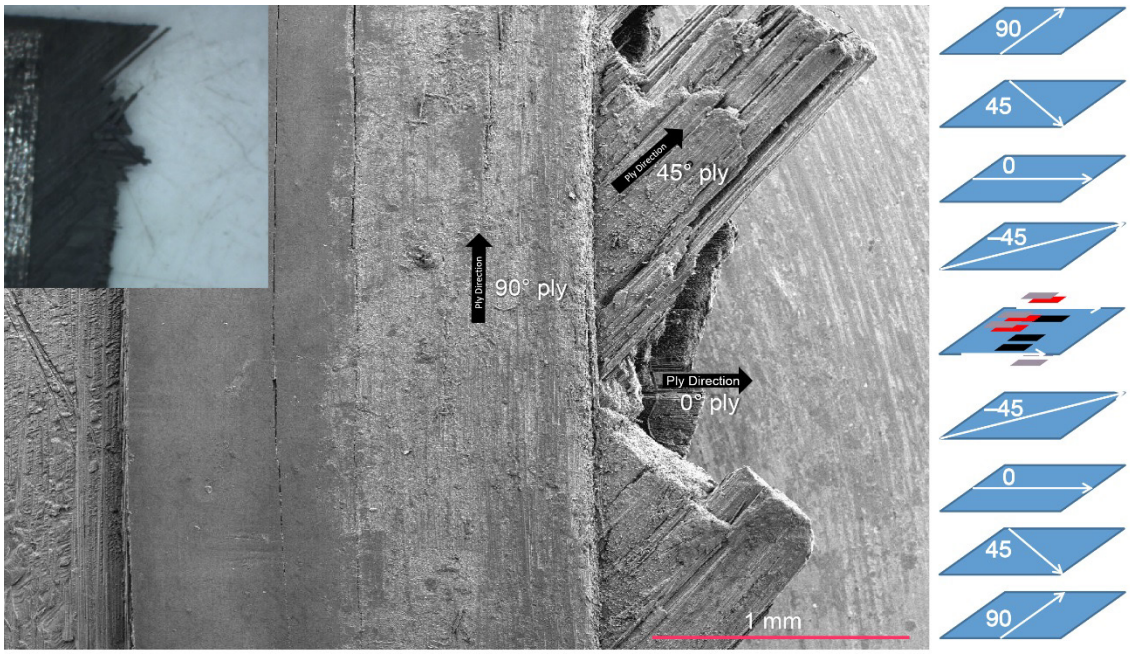

Figure 26.—Analysis of ply fracture pattern in layup 3—(90/+45/0/-45/0/-45/0/+45/90).

5.2.2 Idealized Burst/Delamination Schematics

These layups and their break patterns can be further realized through idealized schematics. Figure 27 shows the burst/delamination pattern for the first layup series. In this image, the first breaks occurred at the inner 90° plies, and traversed both towards the outer edge of the part and caused delamination along the border of the 90° ply. This is verified in Figure 22 and Figure 23. This failure, while not entirely detrimental due to the placement of an SMA section in the middle, is still not ideal; the delaminations could easily cross into the epoxy-rich areas surrounding the SMA material.

The burst/break patterns for layup 2 is visualized in Figure 28. In this figure, the crack once again begins within the epoxy matrix of the 90° ply. Delaminations occurred between the 90° plies, bordering the ±45° plies. Ultimate failure throughout the part was extremely violent, due to the amount of force required to break the fibers of the triple 0° ply interior in tension. The delamination propagation is verified in Figure 23, where delaminations failed to traverse to the interior section of the specimen. The violent burst/break pattern of the entire specimen is verified in Figure 24, where the majority of plies could not be seen from the break surface and again in Figure 6, where macroscopic images show the location of fibers and their random breaks along with large crack through the interior triple 0° ply. The insertion of an SMA section within the triple 0° ply layer is considered ideal. Delamination along this central layer would not occur, and breaks within this layer would also not occur until the fibers aligned in the direction of the force also underwent breakage at a fairly high load.

Figure 29 visualizes the third layup sequence. In this image, the crack propagation direction is found to be inwards due to the breaks first appearing on the surface of the 90° plies. This is verified in Figure 26; the break was clean throughout the specimen, with some minor breaks travelling through the exterior 90° ply. The random nature of the delaminations in Figure 7 are verified in Figure 25; delaminations observed via SEM do not travel solely along the outer 90° plies, but they travel randomly throughout the interior of the entire specimen. This is opposite of the break itself; which is fairly “clean” and occurs through the part in one major section. Insertion of an SMA section within the third layup sequence may give good strength due to failure in one section, but the scattering of delaminations throughout several plies at once could be further aggravated by the resin-rich areas surrounding the SMA insert.

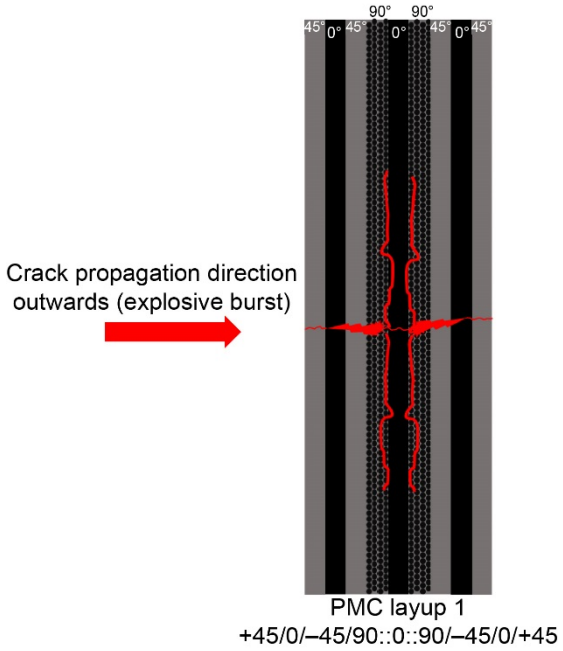

Figure 27.—Burst-failure and delamination graphic for layup 1.

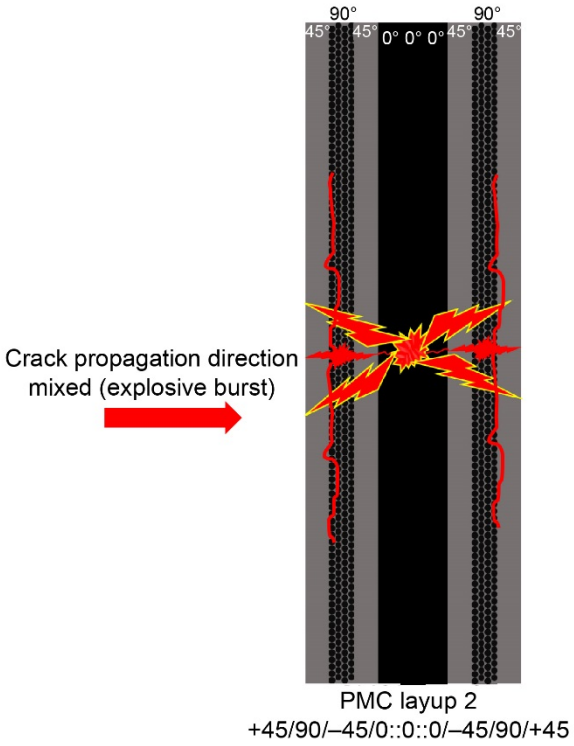

Figure 28.—Burst-failure and delamination graphic for layup 2.

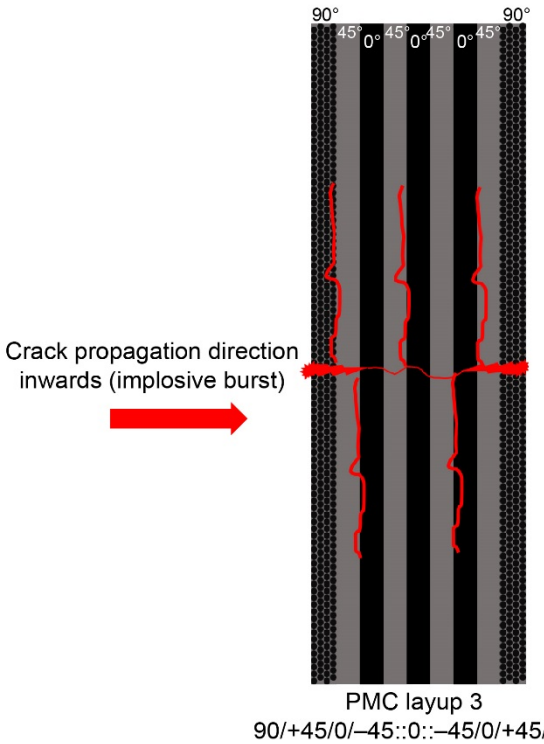

Figure 29.—Burst-failure graphic for layup 3.

5.3 Mechanical Properties

Three major mechanical properties were determined from the tensile testing data—the ultimate tensile strength, ultimate engineering tensile strain, and chord modulus. These results are shown in Figure 16 to Figure 18. Due to similar layups between specimens, it was originally hypothesized that the majority of tensile results would be similar, with trends emerging from the use of adhesives within certain specimen sets. This was not the case for all results presented in this paper.

Predictably, the materials specimen with the highest tensile strength (744.24 MPa) in Figure 16 was a control series with no SMA material. Specifically, the control specimens contained a triple 0° ply directly in the center. Looking at the standard deviation values within the control series, however, shows that these sets of tests were all statistically in the range with each other. The rest of the samples with SMA strips within them did not show any type of patterns in tensile strength. In fact, the strongest sample with the SMA strip did not have any added adhesive, while the weakest sample was with additional adhesive. It can be summarized that the use of additional of adhesives can actually be detrimental to the specimen if proper adhesive selection and SMA surface treatment is not used.

The values of ultimate engineering tensile strains in Figure 17 show a much different set of results than the tensile strength itself. Once again, the control series without SMA performed statistically similar in terms of strain. For the rest of the samples with embedded SMA, the samples with a triple 0° ply layer had significantly higher strain values than other layups. The addition of adhesive to the SMA within these bonding scenarios increased the strain further, though the standard deviations were also much higher. It can be resolved that strengthening the central 0° triple ply layer led to an increase in the overall strain values.

The values of chord modulus presented in Figure 18 were exactly the opposite of the trend observed for strain data; the control sample with the 0° triple ply layer was the stiffest series without SMA material, while the SMA specimen all showed the opposite effect. No matter what adhesive was used, when an SMA insert was present, the 0° triple ply layer were always the most compliant. This effect was reduced when the adhesive was added, but the trend still continued. The standard deviations values for these samples were all high.

5.4 Acoustic Properties

The use of modal acoustic emissions was originally intended to determine if an optimal layup configuration existed for the purpose of resolving failure location within a specimen. More specifically, the use of AE location would be used to see when the SMA section within a specimen would fail. The issue that arose during testing is that only 29 of the 45 specimens tested with SMA inserts actually failed at the gage area; the rest failed near the grip sections.

5.4.1 AE Strength and Location

An example of location of AE failure correlated to the values of stress and time is shown in Figure 19. Analysis of all generated graphs showed three specific trends in the AE data.

These trends were based on the location of the 90° plies. Data from specimens B-1, D-3 and L-1 were chosen to show how the placement of 90° plies resulted in three different AE patterns. AE location data is shown for these specimens in Figure 30. These graphs improve upon the data shown in Figure 19 by plotting the location of AE events along with identifying the “strength” of these events. Strength of AE signals was divided into three categories; small events (<1 V^2-s), medium events (1-10 V^2-s) and large events (>10 V^2-s).

Figure 30(a) shows a moderate amount of AE signals, with most ranging in the “middle” in terms of AE strength. The placement of 90° plies within the mid-plane of the PMC plies is the cause of this. Placement of the 90° plies near the center of the specimen, such as shown in Figure 30(b), reveals that the amount and strength of AE signals is minimized. Placement of the 90° plies on the outside of the samples, such as shown in Figure 30(c), maximizes the amount and strength of AE signals generated.

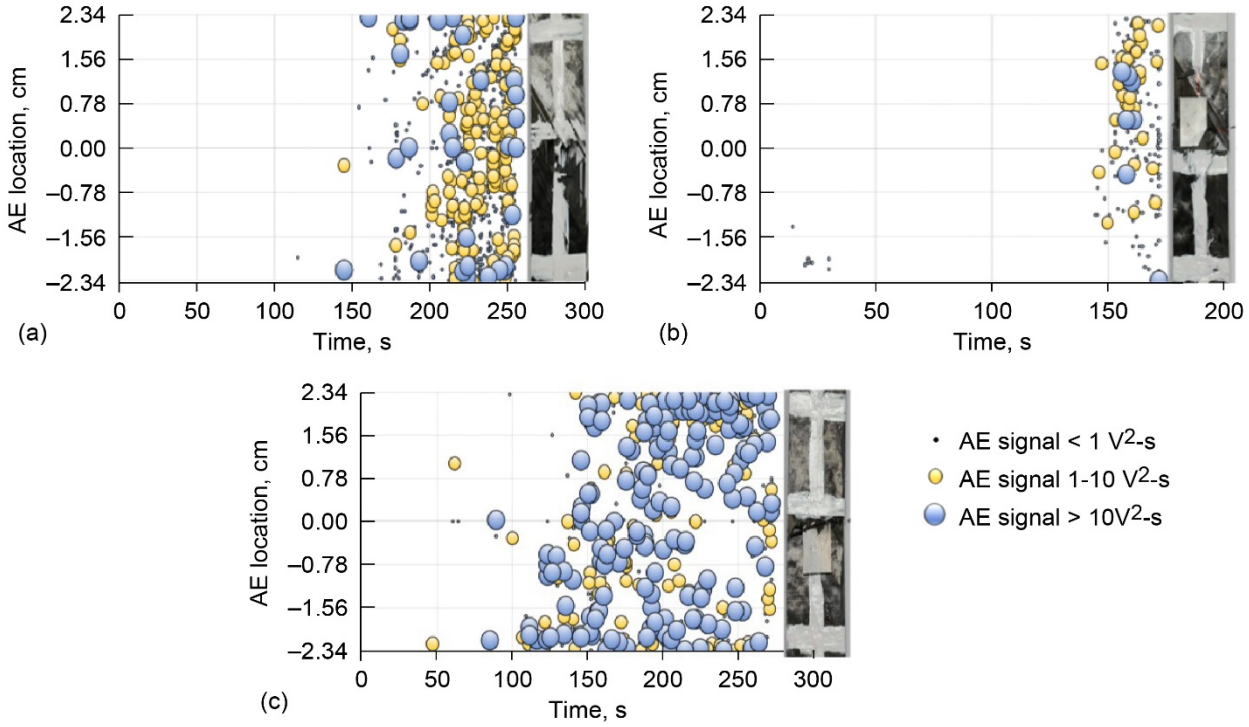

Figure 30.—AE strength and location plots for specimens (a) B-1, (b) D-3, and (c) L-1.

The changes in AE signal strength and amount can be explained by Modal Acoustic Emission theory, which has been previously applied to waveforms generated from a variety of events occurring throughout the mechanical failure of a PMC (Refs. 28, 35 to 38). A surface crack will generate a low frequency flexural (antisymmetric) waveform due to a bending moment associated with an off-center crack. An interior 90° ply transverse crack will generate a high frequency extensional (symmetric) waveform, due to the axial-directed pressure associated with a 90° ply transverse crack that is near the center of the specimen. This theory is shown by graphs in Figure 30.

Along with two-dimensional location of the AE signals between the outer sensors, analysis of the waveform frequencies generated can reveal where cracking was initiated in a sample. As previously described, surface cracks will generate low frequency waveforms, while interior cracks will generate high frequency waveforms. By looking at the first and last waveforms generated during testing, it can be revealed whether the specimens began cracking from the interior or exterior, as shown in Figure 27 to Figure 29. Figure 31 shows waveform frequencies generated at the beginning and end of testing for specimens B-1, D-3, and L-1.

Figure 31(a) shows one of the first waveforms generated during B-1 specimen testing, while Figure 31(b) shows one of the last waveforms generated during B-1 specimen testing. The majority of waveforms that first occurred within specimen B-1 were similar to image A; high frequency waveforms. The majority of waveforms that occurred near the end of testing of specimen B-1 were similar to Figure 31(b); low frequency waveforms. This change in frequency indicates that the initial cracks in specimen B-1 took place within the interior of the specimen, as shown in Figure 28.

The same case is shown for specimen D-3 in Figure 31(c) and (d). The majority of waveforms to first occur within specimen D-3 were similar to Figure 31(c); high frequency waveforms. The majority of waveforms to occur last within specimen D-3 were similar to Figure 31(d); low frequency waveforms. This change in frequency indicates that the initial cracks in specimen D-3 took place within the specimen, as shown in Figure 27.

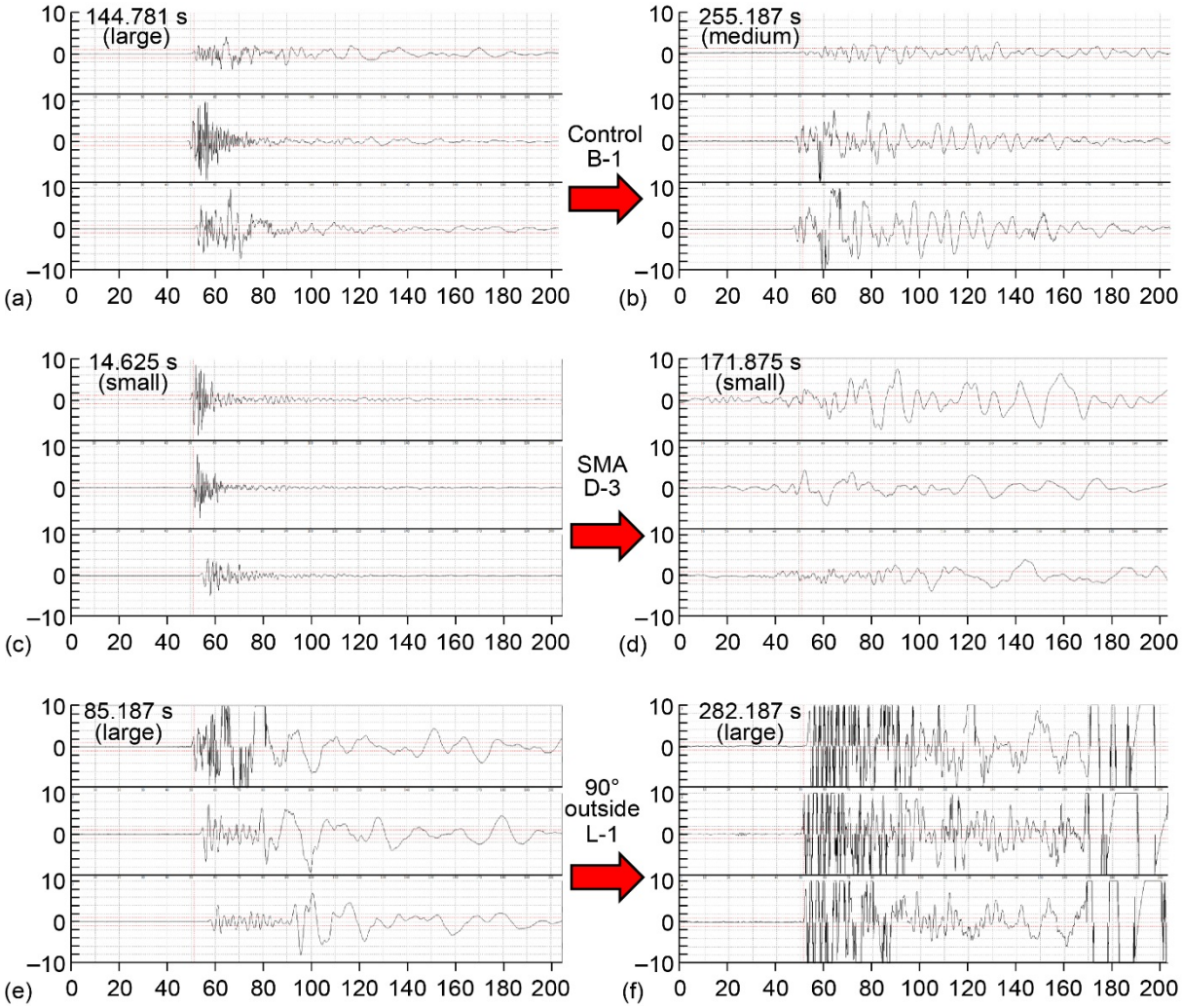

Figure 31.—Waveform frequencies for specimens (a,b) B-1, (c,d) D-3, and (e,f) L-1.

Figure 31(e) and (f) for specimen L-1 are opposite of the trends shown in Figure 31(a) to (d). In these images, low frequency waveforms occurred at the beginning of testing for specimen L-1, while high frequency waveforms occurred near the end of testing. This is shown in Figure 29, and helps prove the theory that the 90° plies located on the outside of the specimen are where the first cracks begin to propagate on the test specimen.

6.0 Conclusion

This study examined the interaction between SMA adhesion with PMC's along with the effect that PMC layups would have on this bonding. Three different bonding scenarios, along with three different layups were utilized and tested in tensile modes. During testing, these specimens were monitored with acoustic sensors; these AE signals were then plotted against the stresses in the systems along with break locations during sample failure.

Without any preparation of the SMA surfaces, the bond layer between PMC and SMA was not affected greatly by the addition of adhesives. There were no obvious trends in mechanical properties based on either the layup or adhesive used; the only real trend that occurred in data was more dependent on the presence of a triple layer of fibers oriented in the direction of the tensile force. The only downside to the triple layer of fibers was the explosive break that occurred during failure, which would result in a

more difficult repair if this were an actuator in use. This central triple ply layer, however, was extremely resistant to delaminations caused by tensile forces; this would be an ideal use for SMA insertion within a PMC being loaded in some form of tension.

The behavior of the central SMA-embedded ply was (mechanically) the most important information derived from this study; follow up studies would likely compare how the fiber direction of the ply the SMA is embedded within differs mechanically. The insertion of an SMA capable of shape change within a PMC actuator may call for specifically oriented ply layers that the SMA is in line with. This, along with proper surface preparation and adhesives used would result in an SMA-PMC hybrid specimen capable of repeated actuation with minimal damage to the part.

Acoustic signals monitored during mechanical failure of specimens reacted as predicted by various other papers (Refs. 28, 35 to 38); the presence of 90° plies (and their location within the various layups) determined the amount and strength of cumulative AE energy detected during testing. AE location equations (Ref. 27) were utilized in order to match acoustic signals along with specific times, stresses and locations on the parts. The frequency of AE wave data helped show whether failure began on the interior or exterior of the tested specimens. The overall data generated from AE analysis was successful in displaying where failure would occur in the part, no matter what layup configuration was used.

References

1. Bollas, D: Stress Generation by shape memory alloy wires embedded in polymer composites. *Acta Materiala* 2007, *55*, 5489–5499.
2. Parthenios, J: Adaptive composites incorporating shape memory alloy wires. *Composites: Part A* 2001, *32*, 1735–1747.
3. Turner, T: Fabrication and Characterization of SMA hybrid composites. *Smart Structures and Materials* 2001, *343*, 33–43.
4. Hisaaki, T; Elzbieta, P; Yoshihiro, E; Toshimi, S: Thermomechanical Properties of Shape-Memory Alloy and Polymer and Their Composites. *Mechanics of Advanced Materials and Structures* 2009, *16*, 236–247.
5. Araujo, CJ: Fabrication and static characterization of carbon-fiber-reinforced polymers with embedded NiTiNOL shape memory wire actuators. *Smart Materials and Structures* 2008, *17*, 6.
6. Poon, C; Zhou, L; Jin, W; Shi, S: Interfacial Debond of Shape Memory Alloy Composites. *Smart Material Structures* 2005, *14*, 29–37.
7. Schrooten, J: Progress on Composites with Embedded Shape Memory Alloy wires, *Materials Transactions* 2002, 43, 1–13.
8. Kim, C; Park, B-S; Goo, N-S: Shape Changes by Coupled Bending and Twisting of Shape-Memory-Alloy Embedded Composite Beams. *Smart Material Structures* 2002, *11*, 519–526.
9. Ostachowicz, W: Dynamics and buckling of a multilayer composite plate with embedded SMA wires. *Composite Structures* 2000, *48*, 163–167.
10. Turner, T; Buehrle, R; Cano, R; Fleming, G: Modeling, fabrication, and testing of a SMA hybrid composite jet engine chevron concept. *Journal of Intelligent Material Systems and Structures* 2006, *17*, 483–497.
11. Song, G; Kelly, B; Agrawal, BN; Lam, PC; Srivatsan, TS: Application of shape memory alloy wire actuator for precision position control of a composite beam. *Journal of Material Engineering Performance* 2000, *9*, 330–333.
12. Lagoudas, DC: Modeling of a flexible beam actuated by shape memory alloy wires. *Smart Material Structures* 1997, *6*, 265–277.
13. Hebda, DA; White, S.R.: Structural behavior of SMA composite beams. *Adaptive Material Systems* 1995, *206*, 111–119.
14. Duering, TW; Melton, KN; Stockel, D: Engineering Aspects of Shape Memory Alloys. London: *Butterworth-Heinemann*, 1990.

15. J.S.N, Paine; C.A., Rogers: Review of multi-functional SMA hybrid composites materials and their applications. *Adaptive Structures and Composite Materials: Analysis and Application* 1994, *54*, 37–45.
16. Xu, Y; Otsuka, K; Yoshida, H; Nagai, H; Oishi, R; Horikawa, H; Kishi, T: A New Method for Fabricating SMA/CFRP Smart Hybrid Composites. *Intermetallics* 2002, *10*, 361–369.
17. Jang, BK; Kishi, T: Thermomechanical Response of TiNi Fiber-Impregnated CFRP composites. *Material Letters* 2005, *59*, 2472–2475.
18. ASTM D3039/D3039M – 08: Standard Test Method for Tensile Properties of Polymer Matrix Composite Materials.
19. *Hexply 8552*; MSDS No. FTA 072e [Online]; Hexcel Composites, February 2013 http://www.hexcel.com/Resources/DataSheets/Prepreg-Data-Sheets/8552_eu.pdf (accessed May 2015).
20. *Loctite Hysol EA 9696*; ID No. AF9118512 [Online]; Henkel Adhesives, April 2007 http://hybris.cms.henkel.com/henkel/msdspdf?matnr=698917&country=US&language=EN (accessed May 2015).
21. *Cytec FM 377U;* ID No. AEAD-00014 [Online]; Cytec Adhesives, April 2010 http://www.cytec.com/sites/default/files/datasheets/FM_377_040710.pdf (accessed May 2015).
22. *3M Scotch-Weld Structural Adhesive Film AF 163-2;* ID No. 62319253092, November 2009 http://multimedia.3m.com/mws/media/282041O/3m-scotch-weld-structural-adhesive-film-af-163-2-af-163-3.pdf (accessed May 2015).
23. De Groot, PJ; Winjem, PAM; Janssen, RBF: Real-time frequency determination of acoustic emission for different fracture mechanisms in carbon/epoxy composites. *Composites Science and Technology* 1995, *55*, 405–412.
24. Gutkin, R; Green, CJ; Vangrattanachai, S; Pinho, ST; Robinson, P; Curtis, PT: On acoustic emission for failure investigation in CFRP: pattern recognition and peak frequency analyses. *Mechanical System Signal Process* 2011, *25*, 1393–407.
25. Arumugam, V; Sajith, S; Stanley, J: Acoustic emission characterization of failure modes in GFRP laminates under Mode I delamination. *Journal of Nondestructive Evaluation* 2011, *30*, 213–219.
26. Ramirez-Jimenez, C; Papadakis, N; Reynolds, N; Gan, T; Purnell, P; Pharaoh, M: Identification of failure modes in glass/polypropylene composites by means of the primary frequency content of the acoustic emission event. *Composites Science and Technology* 2004, *64*, 1819–1827.
27. Morscher, G: Modal acoustic emission of damage accumulation in a woven SiC/SiC composite. *Composites Science and Technology* 1999, *59*, 687–697.
28. Baker, C; Morscher, M; Pumar, V; Lemanski, J; Transverse cracking in carbon fiber reinforced polymer composites: Modal acoustic emission and peak frequency analysis. *Composites Science and Technology 2015*, *116*, 26–32.
29. Pilato, L; Michno, M: Advanced Composite Materials, New York: *Springer-Verlag Berling Heidelberg Publishing Company* 1994.
30. Yashiro, S; Yoshimura, A; Sakaida, Y: Characterization of high-velocity impact damage in CFRP laminates: Part II – prediction by smoothed particle hydrodynamics. *Composites: Part A* 2014, *56* 308–318.
31. Tanabe, Y; Aoki, M; Fujii, K; Kasano, H; Yasuda, E: Fracture behavior of CFRPs impacted by relatively high-velocity steel sphere. *International Journal of Impact Engineering* 2003, *28*, 627–642.
32. Wisnom, MR; Haberle, J: Prediction of buckling and failure of unidirectional carbon fibre/epoxy struts. *Composites Structures* 1994, *28*, 229–239.
33. Fuwa, M; Bunsell, AR; Harris, B: Tensile failure mechanisms in carbon fibre reinforced plastics. *Journal of Materials Science* 1975, *10*, 2062–2070.
34. Gergely, J; Pantelides, C; Reaveley, L: Shear Strengthening of RCT-Joints Using CFRP Composites. *Journal of Composites for Construction* 2000, *4*, 56–64.

35. De Baere, I; Paepegem, WV; Quaresimin, M; Degrieck, J: On the tension-tension fatigue behavior of a carbon reinforced thermoplastic part I: Limitations of the ASTM D3039/D3479 standard. *Polymer Testing* 2011, *30*, 625–632.
36. Surgeon, M; Wevers, M: Modal analysis of acoustic emission signals from CFRP laminates. *NDT&E International* 1999, *32*, 311–322.
37. Prosser, WH; Jackson, KE; Kellas, S; Smith, BR; McKeon, J; Friedman, A: Advanced waveform based acoustic emission detection of matrix cracking in composites. *NASA Langley Technical Report Server* 1995.
38. Gorman, MR: Modal AE: a new understanding of acoustic emissions. *Journal of Acoustic Emission* 1996, *14*, 96–1002.